Aberration-corrected cryoimmersion light microscopy

Raffaele Faoro[a,1], Margherita Bassu[a,1], Yara X. Mejia[a], Till Stephan[b], Nikunj Dudani[a], Christian Boeker[c], Stefan Jakobs[b,d], and Thomas P. Burg[a,2]

[a]Biological Micro- and Nanotechnology, Max Planck Institute for Biophysical Chemistry, Göttingen 37073, Germany; [b]Structure and Dynamics of Mitochondria, Max Planck Institute for Biophysical Chemistry, Göttingen 37073, Germany; [c]Carl Zeiss Microscopy GmbH, Göttingen 37081, Germany; and [d]Department of Neurology, University Medical Center Göttingen, Göttingen 37073, Germany

Edited by David J. DeRosier, Brandeis University, Waltham, MA, and approved December 15, 2017 (received for review October 2, 2017)

Cryogenic fluorescent light microscopy of flash-frozen cells stands out by artifact-free fixation and very little photobleaching of the fluorophores used. To attain the highest level of resolution, aberration-free immersion objectives with accurately matched immersion media are required, but both do not exist for imaging below the glass-transition temperature of water. Here, we resolve this challenge by combining a cryoimmersion medium, HFE-7200, which matches the refractive index of room-temperature water, with a technological concept in which the body of the objective and the front lens are not in thermal equilibrium. We implemented this concept by replacing the metallic front-lens mount of a standard bioimaging water immersion objective with an insulating ceramic mount heated around its perimeter. In this way, the objective metal housing can be maintained at room temperature, while creating a thermally shielded cold microenvironment around the sample and front lens. To demonstrate the range of potential applications, we show that our method can provide superior contrast in *Escherichia coli* and yeast cells expressing fluorescent proteins and resolve submicrometer structures in multicolor immunolabeled human bone osteosarcoma epithelial (U2OS) cells at −140 °C.

cryo-light microscopy | high-*NA* immersion objective | fluorescence imaging | cryofixation | cryofluorescence microscopy

Fluorescent light microscopy at cryogenic temperature presents significant advantages in itself and provides an important complement to electron cryomicroscopy (1, 2). In particular, bleaching decreases drastically at low temperature (3), while the fluorescence yield of many fluorophores increases (4), and the spectral bands narrow (5–8). The application of modern superresolution methods such as stimulated emission depletion microscopy (STED) (9), photoactivated localization microscopy (10), stochastic optical reconstruction microscopy (11), or structured illumination microscopy (12) at cryogenic temperature holds the prospect of imaging fluorescent proteins with high precision in 3D and correlating their localization with the ultrastructure seen in electron cryomicroscopy of the same sample (3, 4, 13–16). In contrast to chemical fixation, cryofixation provides an unbiased, undistorted representation of the native state. This is increasingly more important as imaging resolution approaches the nanometer scale.

A long-standing challenge in cryogenic light microscopy is the lack of high-numerical-aperture (*NA*) microscope objectives. The *NA* of an objective is the primary figure of merit that dictates its light-collection efficiency and diffraction-limited resolution. Significant technological development has been devoted toward user-friendly platforms based on high-*NA* air objectives optimized for cryomicroscopy (17–19). However, air objectives are fundamentally limited to *NA* values <1.

Immersion objectives can surpass this limit by making physical contact with the sample via an immersion medium of refractive index >1. At room temperature, this is a cornerstone of practically all high-resolution light microscopy, but for imaging below the glass transition of water (~ -135 °C), no satisfactory counterpart exists.

Two different approaches toward cryoimmersion light microscopy have been proposed in the past. The first is to cool the sample and the objective to cryogenic temperature, thereby avoiding thermal gradients in the system. This approach was followed by Larabell and coworkers (20–22) and by Brecht and coworkers (8). Both used inexpensive oil-immersion objectives that could sustain the deep temperature cycles without damage. However, this approach has never been shown to work with sophisticated bioimaging immersion objectives. Such objectives rely on numerous glued and often adjustable lens groups that would require an elaborate redesign for temperatures below -135 °C. A second challenge is that no adequate index-matching media are available for this temperature range. Aberration-free imaging requires the refractive index to be within at least $\sim 10^{-3}$ refractive index unit (RIU) of the design value for the objective. In addition, the medium needs to be optically clear, nonfluorescent, and nontoxic, and have low vapor pressure at the imaging temperature. Facile storage and handling, moreover, require that the liquid range should extend above room temperature. Although Brecht and coworkers found that 1-propanol (melting point -126 °C) satisfies many of these criteria at -110 °C, this is still significantly above the glass transition of water and cannot be generalized to lower temperatures.

In the second approach described in the literature, the objective remains warm while a temperature drop of >150 °C is maintained between the sample and the front lens (23). Nahmani et al. accomplished this by injecting a continuous stream of a warm ethanol/water mixture (70% ethanol) between the front lens and a coverslip placed on top of the cryogenically cooled sample. Although freezing was successfully prevented, the

Significance

Cryofluorescence imaging is of great interest in biological microscopy because vitrified samples (i.e., frozen without ice crystallization) are free from fixation artifacts, are highly photostable, and allow direct correlation with electron cryomicroscopy. Here, we show a concept for conducting cryo-light microscopy in immersion that provides a twofold to fivefold increase in image brightness and higher resolution than are attainable with air objectives. Spherical aberration at an imaging temperature below the glass transition of water (−135 °C) is corrected by our approach.

Author contributions: R.F., M.B., Y.X.M., S.J., and T.P.B. designed research; R.F., M.B., Y.X.M., T.S., and N.D. performed research; C.B. supervised the implementation of the prototype objective; T.P.B. designed the project; R.F., M.B., T.S., S.J., and T.P.B. analyzed data; and R.F., M.B., S.J., and T.P.B. wrote the paper.

The authors declare no conflict of interest.

This article is a PNAS Direct Submission.

[1]R.F. and M.B. contributed equally to this work.

[2]To whom correspondence should be addressed. Email: tburg@mpibpc.mpg.de.

This article contains supporting information online at www.pnas.org/lookup/suppl/doi:10.1073/pnas.1717282115/-/DCSupplemental.

refractive index of the ethanol/water mixture did not match the design of the objective. In general, attaining an accurate and stable index match in this technique is complicated by the presence of thermal boundary layers and the potential for pressure-induced artifacts.

In this work, we describe an approach toward immersion light microscopy at −140 °C that combines a cryoimmersion medium, HFE-7200, which matches the refractive index of room-temperature water at cryogenic temperature with a technological concept in which the objective itself is not in thermal equilibrium. The temperature drop is maintained by actively heating the ceramic lens mount along the perimeter near its connection with the objective body (Fig. 1). Differently from the approach patented by Le Gros and Larabell (22), in our method, the objective metal housing is maintained at room temperature, thus reducing the risk of damaging the numerous lenses composing the bioimaging objective. At the same time, a thermally shielded microenvironment is created around the sample and front lens. An important advantage of our approach is that refractive index gradients due to temperature variations in the liquid are small and not likely to distort the wavefront.

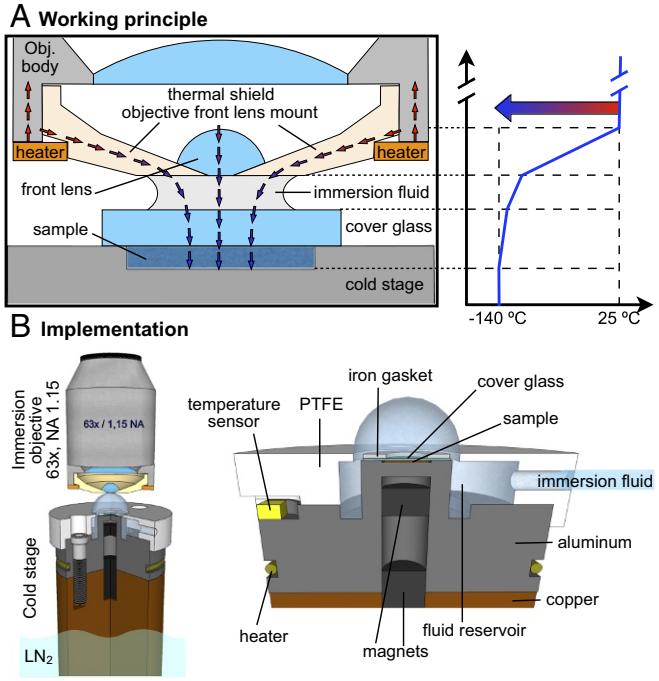

Fig. 1. (*A*) Schematic cross-section of an immersion objective with the front lens mount made of Macor operating as a thermal shield. The heat flows across the sample, cover glass, immersion fluid, front lens, and ceramic mount. The low thermal expansion coefficient of the machinable ceramic allows for reducing the thermal stresses. The high thermal resistance of Macor allows confining most of the temperature gradient in the front lens mount, as shown in the diagram. Note that due to the high thermal conductivity of the metallic cold stage and the intimate contact with the sample, the stage temperature closely reflects the temperature of the sample. (*B*) The cold stage used for the implementation of cryoimmersion microscopy was designed to keep both sample and cryoimmersion fluid at a stable temperature by combining heating and temperature sensing. The stage is composed of two parts, a bottom copper bar, which is in direct contact with liquid nitrogen, and a top anodized aluminum post. The sample is placed on top of the aluminum post and is in direct contact with the metal below a coverslip. The coverslip and sample are secured magnetically to the post by using an iron gasket and a magnet glued inside the aluminum post. The immersion fluid is supplied to the reservoir through a channel in the polytetrafluoroethylene (PTFE) cap. The opening in the PTFE cap allows forming a cold drop around the sample.

To implement this approach, we prototyped a cryoimmersion objective starting from a commercial water immersion bioimaging objective (Zeiss LD C-Apochromat 63×, $NA = 1.15$). We chose this objective mainly for (*i*) its long working distance (600 μm), which helps to minimize heat transfer to the sample, and (*ii*) the built-in correction collar, which can be used to correct residual spherical aberration. To prevent condensation and frost build-up, the interior of the objective was purged continuously with dry nitrogen gas. This was made possible by custom-integrated channels, which traversed the objective body and ended with holes in the Macor front lens mount. To maintain the objective at 25 °C, all heat losses were compensated by an electrically heated copper ring attached near the transition between the ceramic front lens mount and the metallic housing of the objective.

Searching for a suitable immersion medium, we discovered that the partially fluorinated liquid ethoxynonafluorobutane (3M HFE-7200), has a surprisingly low refractive index (1.28) at room temperature and a liquid range from > 70 °C to below −140 °C. Note that HFE-7200 is also inexpensive, nontoxic, and safe for the environment.

Combining our cryoimmersion objective with the optical properties of HFE-7200, we were able to perform fluorescence cryomicroscopy free from spherical aberrations at −140 °C (Fig. 2*A*).

To find the optimal working temperature, we compared the point spread function (PSF) of our objective with HFE-7200 immersion to the PSF at room temperature using the standard medium (Zeiss W2010, $n = 1.334$) (Fig. 2*B*). As a reference, we also compared the results with the performance of an air objective (Zeiss LD Achroplan 63 × /0.75; working distance 2.8 mm) in cryoconditions and at room temperature (Fig. 2 *E* and *F* and Table 1). In comparing the performance of different objectives at different temperatures, it was helpful to consider resolution and light collection efficiency independently, as both depend not only on characteristics of the objective, but also on characteristics of the sample and the stage under different conditions.

The overall shape and symmetry of the PSFs are very similar at −140 °C (HFE-7200) and at 23 °C (Zeiss W2010), indicating that the refractive index of HFE-7200 is well matched to the design of the objective at this temperature. Importantly, the PSFs were very uniform across the entire field of view (2D heat maps in Fig. 2), which is critical in widefield and beam-scanning microscopy techniques. The symmetry of the PSFs and their uniformity over the field indicated that there were no significant lateral refractive index gradients in the medium.

To assess the level of index-matching more quantitatively, we conducted various measurements of the PSF with purposely mismatched conditions. At room temperature, using a 6% glycerol solution ($n = 1.337$) produces significant positive spherical aberration, as seen in Fig. 2*C*. In cryoconditions, we observed increasing negative spherical aberration when the temperature was raised from −140 °C over −130 °C (Fig. S1) to −90 °C (Fig. 2*D*).

One of the key advantages of immersion objectives over air objectives is their light collection efficiency, which grows as $\sim NA^2$. Indeed, we measured an increase in brightness of 5.7 ± 0.6 times from a 63 × /0.75 air objective to our 63 × /1.15 immersion objective at −140 °C. This was in agreement with the expected scale factor of $\sim NA^4$ for widefield fluorescence imaging. If an objective with a *NA* of 0.9 had been used in our comparison, we would therefore expect that a commensurate increase in brightness of ∼2.7 would have been observed. Thus, it is expected that, in terms of image brightness, cryoimmersion microscopy can provide a significant gain even over the most advanced light cryomicroscopes using air objectives.

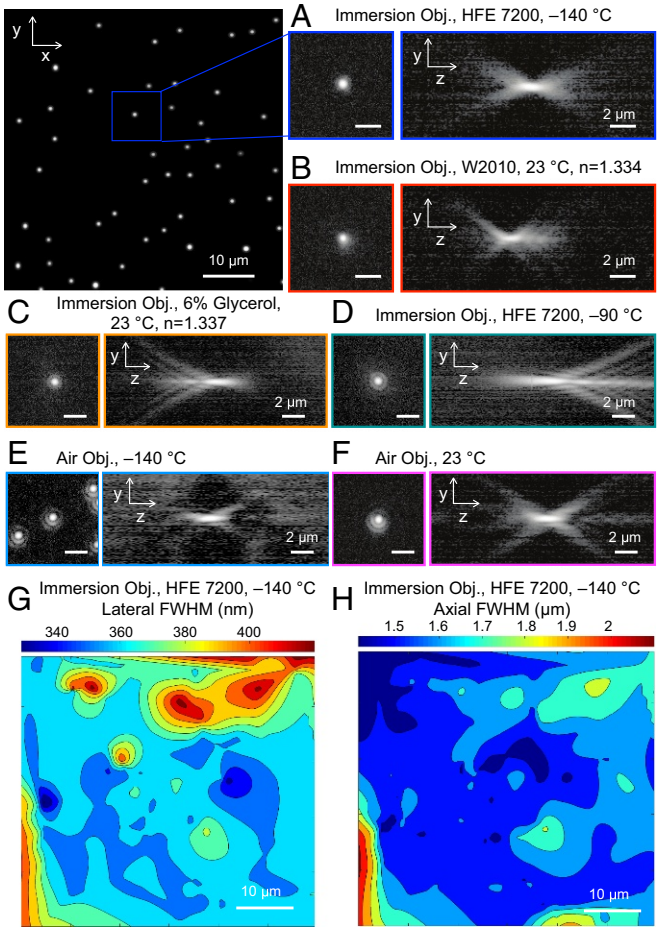

Fig. 2. (*A*) Lateral and axial PSF measured at −140 °C with the cryoimmersion objective (Obj.) and the immersion fluid HFE-7200. Fitting the PSF to a two-dimensional (2D) Gaussian (Fig. S2) allows us to determine lateral and axial resolution. The intensity is normalized and shown on a logarithmic scale. (*B*) Lateral and axial PSF measured at room temperature with the cryoimmersion objective and the commercial immersion fluid W2010. (*C*) Lateral and axial PSF measured at room temperature with the cryoimmersion objective and 6% glycerol ($n = 1.337$) as immersion fluid. The refractive index mismatch produces positive spherical aberrations. (*D*) Lateral and axial PSF measured at −90 °C with the cryoimmersion objective and the immersion fluid HFE-7200. The refractive index of the immersion fluid at −90 °C is smaller than the refractive index of water at room temperature, producing negative spherical aberrations. (*E*) Lateral and axial PSF measured at −140 °C with the 0.75-*NA* air objective. (*F*) Lateral and axial PSF measured at room temperature with the air objective. (All scale bars in *A*–*F* are 2 μm.) (*G*) A 2D heat map of the measured lateral FWHM at −140 °C. (*H*) A 2D heat map of the measured axial FWHM at −140 °C.

In order to demonstrate applications of our method, we imaged *E. coli* cells expressing green fluorescent protein (GFP), yeast cells expressing GFP tagged to the eisosome core component Pil1, and immunostained human bone osteosarcoma epithelial cells (U2OS) (Fig. 3). *E. coli* and yeast cells were imaged in both live ambient conditions and after plunge freezing in cryoconditions.

The benefits of cryofixation and imaging in cryoconditions were particularly evident for yeast cells (Fig. 3*C*). A considerable improvement of both signal-to-noise ratio and image quality was achieved in cryoconditions where the photobleaching was suppressed ∼64 times (Fig. 3*D*). In the cryofixed cells, a fluorescence signal also appeared at locations that are dark at room temperature. This could have been due to an increase in the autofluorescence of some biomolecules at low temperature or due to alterations introduced during sample preparation and plunge freezing. No particular structural differences were appreciable in images of live *E. coli* and cryofixed *E. coli* (Fig. 3*A*). GFP expressed in bacteria bleaches relatively slowly already at room temperature, and the rate was suppressed only by a factor of 3.5 in cryoconditions (Fig. 3*B*).

Next, we established the possibility of resolving submicrometer cell structures by multicolor cryofluorescence microscopy using our method. Fig. 3 illustrates the attainable image quality in widefield fluorescence of immunostained U2OS cells at −140 °C. Networks of mitochondria (Tom20 immunolabeled with Alexa Fluor 594-decorated antibodies) and vimentin filaments (Alexa Fluor 488) were well resolved simultaneously. This surprising finding indicates that the chromatic dispersion of HFE-7200 must also be in close match to the designed correction of the objective. However, more detailed measurements will be needed to assess lateral and axial chromatic aberrations quantitatively.

In conclusion, we demonstrated a concept to approach diffraction-limited performance in high-*NA* cryofluorescence microscopy with commercially available immersion objectives. To achieve this, we created a thermally shielded microenvironment around the sample by replacing the metallic front lens mount of the objective with an insulating ceramic mount that was heated around its perimeter. A further enabling step was our discovery of an immersion medium, HFE-7200, that provided accurate index matching at a sample temperature below the glass transition of water. It was surprising that, although the front lens of the objective was made from two separate elements bonded by an adhesive, we did not observe any damage throughout hundreds of hours of use. The bond between the front lens and the ceramic lens mount also remained stable. This was likely the case because all glued components had very similar thermal expansion coefficients and were only a few millimeters in size. Moreover, the objective lens did not suffer from condensation in spaces between elements.

Some limitations of our method remain to be addressed. First, the objective we used in this work only provides an *NA* of 1.15. While we expect that our approach of thermally isolating the front lens will also work for oil objectives with $NA > 1.4$, new immersion media would then need to be identified. This is likely feasible, as numerous nontoxic fluids with a wide liquid range and a higher refractive index than HFE-7200 exist.

Secondly, the axial and the lateral PSF at low temperature were ∼ 1.7 and ∼ 1.2 times wider, respectively, than at room temperature. We suspect that this was at least partly caused by factors that were unrelated to our cryoimmersion

Table 1. FWHM of the PSF measured in cryoconditions (−140 °C) and at room temperature by using the prototyped cryoimmersion objective (63 × /1.15) and comparison with an air objective (63 × /0.75)

Observation conditions	$FWHM_{xy}$ (nm)	$FWHM_z$ (nm)	Peak intensity (a.u.)
Cryoimmersion objective W2010 @ 23 °C	295 ± 6	902 ± 17	8,444 ± 484
Cryoimmersion objective HFE 7200 @ −140 °C	353 ± 16	1,554 ± 58	3,449 ± 362
Air objective 0.75 *NA* @ −140 °C	385 ± 14	1,743 ± 108	610 ± 165

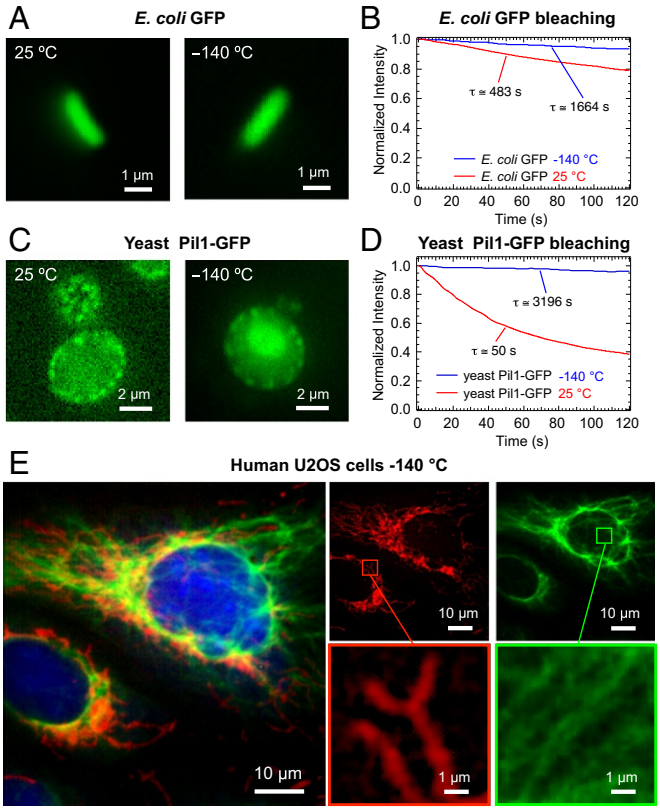

Fig. 3. Imaging of cryofixed biological specimens with the prototyped cryo-immersion objective. (*A*) Room-temperature (*Left*) and cryogenic (*Right*) widefield fluorescence images of *Escherichia coli* expressing GFP. (*B*) Photobleaching curves for GFP expressed in *E. coli*. The red curve shows decay at room temperature, and blue curve shows decay at −140 °C. In cryoconditions, the GFP bleaching is suppressed ∼3.5 times. (*C*) Room-temperature (*Left*) and cryogenic (*Right*) widefield fluorescence images of yeast cells expressing GFP-tagged Pil1. (*D*) Photobleaching curves for GFP expressed in yeast cells. The red curve shows decay at room temperature, and the blue curve shows decay at −140 °C. In cryoconditions, the GFP bleaching is suppressed ∼64 times. (*E*) Three-color widefield cryofluorescence image of plunge frozen U2OS cells labeled with Alexa Fluor 488 (vimentin cytoskeleton), Alexa Fluor 594 (Tom20 mitochondrial protein), and DAPI (cell nuclei).

objective. Importantly, we also found a degradation in resolution between room temperature and cryogenic temperature with our $63\times/0.75$ air objective; similar observations have also been made by other groups using air objectives with *NA* values approaching 0.9 (8). This leads us to believe that the slight degradation in resolution at low temperature may be due to the sample side of the optical system and include stage drift, vibration, or changes in the optical properties upon freezing. Another factor can be the presence of a small axial temperature gradient throughout the immersion medium. This was unavoidable since our method inherently operated away from thermal equilibrium. However, the temperature drop could still be reduced by lowering the temperature of the objective body or by further increasing the thermal resistance of the lens mount. Notably, the light collection efficiency of the objective did not degrade at low temperature, and the increase in brightness with respect to the 0.75-*NA* objective remained in agreement with the expected NA^4 scale factor.

Thirdly, the temperature of −140 °C at which the aberrations were minimal was quite close to the water glass transition temperature of −135 °C. Overcoming this limitation would require identifying a new immersion medium with a wider liquid range and lower room temperature refractive index than HFE-7200. As an example, mixtures of different fluorinated liquids could be used.

Importantly, the temperature of the holder fluctuated within <1 °C. In addition, our intensity comparisons provide evidence that the continuous heat transfer from the objective does not warm the sample significantly. A significant temperature increase would indeed be measurable as an unexpected increase in the intensity of the fluorescent beads used in our PSF characterization when imaging in immersion. This, however, was not observed. While we are confident that our method allows preserving the amorphous state of biological samples, this will need to be confirmed by further analysis of the observed vitrified samples with cryoelectron microscopy or X-ray scattering.

In the future, we believe that this method will enable the combination of advanced light microscopy, including total internal reflection fluorescence or STED, with electron cryomicroscopy to help elucidate connections between structure and function at the subcellular and molecular scale.

Materials and Methods

Sample Preparation.

Fluorescent nanobeads deposition. Fluorescent beads of diameter $\varnothing$ = 175 nm and emission peak wavelength λ_{em} = 525 nm (Merck Millipore, Estapor®) were deposited on the surface of circular #1.5 coverslips 5 mm in diameter (Engelbrecht GmbH). The coverslips were plasma-cleaned, incubated for 5 min in 1% poly-L-lysine (Sigma-Aldrich), rinsed with deionized (DI) water, and then covered with 25 μL of beads solution (3.4×10^8 pt/mL). The particle suspension was left to dry for 2 h in a vacuum chamber.

E. coli *cell preparation.* For protein expression, the plasmid pQE-31-GFP was transferred into *E. coli* expression strain BL21-CP-RIL. The bacteria were cultured on LB medium agar plates. Fluorescent colonies were selected and further cultured in liquid LB medium. The growth medium was replaced with DI water before ambient condition live imaging or plunge-freezing on Formvar/carbon-coated TEM grids (Plano GmbH). Grids were blotted and plunged in liquid nitrogen-cooled propane by using a homemade freezing device (Fig. S3). Samples were stored submerged in liquid nitrogen for later imaging.

Yeast cells preparation. Yeast cells expressing Pil1–GFP were cultured in liquid yeast extract peptone dextrose medium. The growth medium was replaced with DI water before ambient conditions imaging or plunge freezing. Room-temperature microscopy was performed after attaching living yeast cells on poly-L-lysine (Sigma-Aldrich)-coated coverslips. For the preparation of samples for cryomicroscopy, we used poly-L-lysine–covered sapphire discs, 3-mm diameter, 50 μm thick (Engineering Office M. Wohlwend GmbH). The cells were plunge-frozen in liquid nitrogen-cooled propane. Water in excess was removed with filter paper. Samples were stored submerged in liquid nitrogen for later imaging.

U2OS cell preparation. Human U2OS cells were cultured in DMEM containing high-glucose and GlutaMAX (Thermo Fisher Scientific) supplemented with 100 U/mL penicillin and 100 μg/mL streptomycin (Merck Millipore), 1 mM sodium pyruvate (Sigma-Aldrich), and 10% (vol/vol) FBS (Merck Millipore) at 37 °C and 5% CO_2. Cells were seeded on sapphire crystal discs (Engineering Office M. Wohlwend GmbH) and grown overnight. Cells were fixed with prewarmed 4% formaldehyde in PBS (137 mM NaCl, 2.68 mM KCl, and 10 mM Na_2HPO_4, pH 7.4) for 10 min at 37 °C, extracted with 0.5% (vol/vol) Triton X-100 in PBS, blocked with 5% (wt/vol) BSA in PBS, and incubated with polyclonal antibodies against the mitochondrial protein Tom20 (Santa Cruz Biotechnology) and vimentin (Sigma-Aldrich) for 1 h. After five washing steps with PBS and blocking with 10% (wt/vol) BSA in PBS, primary antibodies were detected with secondary sheep anti-mouse Alexa Fluor 488 antibodies (Invitrogen) or goat anti-rabbit antibodies (Jackson ImmunoResearch Laboratories) custom-labeled with Alexa Fluor 594 (Life Technologies) for 1 h. Samples were washed five times with PBS and covered with PBS containing 2.5 μg/mL DAPI (Sigma-Aldrich). The cells were plunge-frozen in liquid nitrogen-cooled propane. Samples were stored submerged in liquid nitrogen for later imaging.

Optical Setup and Image Acquisition. All experiments were performed with an upright microscope (Zeiss Axio Scope.A1) equipped with a compact mercury light source (HXP 120; LEJ). The mechanical stage of the microscope was replaced with a piezo-stage (3-Axis NanoMax Stage; Thorlabs) mounted on a 30- × 15-cm breadboard (Fig. S4). The breadboard was fixed to the microscope stage carrier. In this configuration, the stage could move in the *x*, *y*,

and z axis with a span of 4 mm. The piezo was used to drive the movement of the stage in the z axis only during imaging. Axial movements during objective approach and focusing were performed by using the focusing drive of the microscope. Both piezo stage and camera were controlled by μ Manager (24).

To minimize accumulation of frost, the stage was surrounded by an acrylic glove box designed to seal around the microscope objectives turret. Nitrogen gas was flushed inside the box to maintain humidity levels of <10% during operation in cryoconditions.

The cold stage, consisting of a metal bar, was suspended inside a liquid nitrogen container. A Macor plate glued around the copper bar was used to fix the bar to a rigid aluminum cantilever moved by the piezo stage using magnets. This configuration allowed minimizing the vibration transferred to the stage by the boiling liquid nitrogen and, at the same time, minimizing the heat transfer to the piezo stage and thus keeping only the metal bar cold.

The metal bar supporting the specimens consisted of a bottom part in copper and a top part in anodized aluminum. A graphite sheet 130 μm thick was placed in between the two parts to maximize the thermal gradient at the junction. The temperature of the top part was controlled by using a PT100 sensor and a NiCr heater. A temperature up to −90 °C could be kept stable by applying a maximum power of 30 W to the heater.

The specimen was placed in direct contact with the protruding anodized aluminum post. A recess (diameter 3.2 mm, depth 100 μm) allowed us to place TEM grids or 50-μm-thick sapphire discs below the cover glass and avoid damaging the biological specimens. Importantly, when imaging biological specimens on TEM grids and sapphire discs, the space between sample carrier and coverglass was filled with cryoimmersion fluid. The sample was secured to the stage by using magnetic fixing of an iron gasket placed on top of the coverglass. For this purpose, a magnet was glued inside the aluminum bar below the sample. The cryofixed samples were transferred from liquid nitrogen to the stage inside the dry box just before imaging. During the transfer, the temperature of the stage was kept at approximately −180°C. After securing the sample to the stage, the temperature was raised to −150 °C, and the immersion fluid was supplied into a reservoir opened in between a PTFE cap and the aluminum top bar after being precooled to −90 °C. The liquid was cooled to the stage temperature while flowing inside a needle inserted in the PTFE cap and in contact with the metal stage. The opening of the cup around the post supporting the specimen made it possible to form a cold liquid drop on top of the sample and to contact the cryoimmersion objective.

The air objective (Zeiss LD Achroplan 63×, $NA = 0.75$, working distance 2.8 mm) and the cryoimmersion objective (Macor front lens mount; Zeiss LD C-Apochromat 63×, $NA = 1.15$) were both mounted on the microscope turret during operation. The cryoimmersion objective was mounted on a specifically designed adapter sealed with a tilted fused silica window and equipped with an inlet tube that allowed flushing nitrogen to purge the interior of the objective continuously. Custom-integrated channels, which traversed the objective body and ended with holes in the Macor front lens mount, allowed us to keep the objective dry. The objective body temperature was maintained at 25 °C by compensating all losses using an electrically heated copper ring attached near the transition between the ceramic front lens mount and the metallic housing of the objective.

Before imaging, the stage was raised slowly to put the front lens of the objective in contact with the immersion fluid. When imaging cryofixed biological samples, the stage temperature was kept at −150 °C during the approach. After ∼10–15 min of allowing the front lens to cool down, the temperature of the stage was raised to −140 °C, and focusing was performed.

PSF Measurements. Fluorescent images of subresolution polystyrene beads of diameter $\varnothing = 175$ nm and emission peak wavelength $\lambda_{em} = 525$ nm (Merck Millipore, Estapor®) were acquired by using a front-illuminated scientific complementary metal–oxide–semiconductor camera with 2,560 × 2,160 6.48-μm pixels (Andor; Neo) mounted on a 2.5× beam expander and the filter set 38HE (Zeiss). Only 50% of the camera frame was used, and the integration time was set to 200 ms for all measurements. Beads were sampled at 200-nm steps along the z axis. PSFs were measured at room temperature for W2010 immersion fluid and 6% glycerol. In cryoconditions, the PSFs were measured for HFE 7200 at temperatures ranging between −90 °C and −140 °C with a step of 10 °C. PSFs for air were measured with the air objective (Zeiss LD Achroplan 63×, $NA = 0.75$, working distance 2.8 mm).

PSFs were measured on the same sample spot for comparing the intensity values. The following method was followed: (*i*) imaging with air objective in ambient conditions; (*ii*) cooling of the stage and imaging with air objective in cryoconditions; (*iii*) injection of HFE-7200 in the stage and imaging with the cryoimmersion objective in cryoconditions; and (*iv*) heating to room temperature of the stage and imaging with cryoimmersion objective with W2010 immersion fluid. HFE 7200 evaporated without leaving traces in a few minutes once the stage reached room temperature, allowing us to put W2010 on top of the sample and to perform imaging at room temperature. Image processing and analysis were carried out by using Fiji (25). FWHM values were measured by using the plugin GDSC SMLN after running an inverted deconvolution run for correcting for finite size of the beads using the plugin Deconvolutionlab2 (26).

Imaging of* E. coli *and yeast cells. Fluorescent images of *E. coli* and yeast cells were acquired by using a back-illuminated EM CCD with 512 × 512 16-μm pixels (Andor; IXON 897), mounted on a 2.5× beam expander, and the filter set 38HE (Zeiss). For *E. coli*, we used an integration time of 10 ms and EM gain 20. For yeast cells, the integration time was raised to 100 ms and the EM gain to 50.

Photobleaching assays were performed at room temperature and at −140 °C by continuously exposing the sample to the light from the HXP 120 mercury source. Images were recorded at 250-ms intervals for a total exposure time of 2 min. We subtracted the average intensity of the background from the average intensity of the signal inside a boundary that contained the entire cell. For images of yeast cells in cryoconditions, this boundary was chosen to contain only the Pil1 spots. To correct for drift, the images were aligned by using the Fiji plugin for the recursive alignment of a stack of images StakReg (27). We calculated the bleaching rate as the integral-tau of the decay curve, defined as $\tau = \int t \cdot I(t)\, dt / \int I(t)\, dt$.

Imaging of U2OS cells. Fluorescent images of immunolabeled human U2OS cells were acquired by using the widefield modality of a white-light confocal microscopy system (Revolution DSD; Andor) equipped with a CCD camera 1,262 × 1,031 6.45-μm pixels (Clara, Andor) and filter set D/F/T (DAPI FITC, and Texas Red). The integration time was set to 2 s for each channel. Image processing and analysis were carried out by using Fiji (25).

ACKNOWLEDGMENTS. We thank the groups for optics design, optics manufacturing, and application support of the Carl Zeiss Microscopy GmbH in Göttingen and the chemistry laboratory of the Carl Zeiss AG in Oberkochen (Germany) for many invaluable contributions. We thank Dietmar Riedel for his help and suggestions in preparing the plunge frozen samples and Stefan W. Hell for many fruitful discussions and continuous encouragement. This work was supported by the Max Planck Society and the Max Planck Institute for Biophysical Chemistry.

1. Kaufmann R, Hagen C, Grünewald K (2014) Fluorescence cryo-microscopy: Current challenges and prospects. *Curr Opin Chem Biol* 20:86–91.
2. Loussert Fonta C, Humbel BM (2015) Correlative microscopy. *Arch Biochem Biophys* 581:98–110.
3. Schwartz CL, Sarbash VI, Ataullakhanov FI, Mcintosh JR, Nicastro D (2007) Cryo-fluorescence microscopy facilitates correlations between light and cryo-electron microscopy and reduces the rate of photobleaching. *J Microsc* 227:98–109.
4. Kaufmann R, et al. (2014) Super-resolution microscopy using standard fluorescent proteins in intact cells under cryo-conditions. *Nano Lett* 14:4171–4175.
5. Moerner WE, Orrit M (1999) Illuminating single molecules in condensed matter. *Science* 283:1670–1676.
6. Kozankiewicz B, Orrit M (2014) Single-molecule photophysics, from cryogenic to ambient conditions. *Chem Soc Rev* 43:1029–1043.
7. Li W, Stein SC, Gregor I, Enderlein J (2015) Ultra-stable and versatile widefield cryo-fluorescence microscope for single-molecule localization with sub-nanometer accuracy. *Opt Express* 23:3770–3783.
8. Metzger M, et al. (2016) Resolution enhancement for low-temperature scanning microscopy by cryo-immersion. *Opt Express* 24:13023–13032.
9. Hell SW, Wichmann J (1994) Breaking the diffraction resolution limit by stimulated-emission - stimulated-emission-depletion fluorescence microscopy. *Opt Lett* 19:780–782.
10. Betzig E, et al. (2006) Imaging intracellular fluorescent proteins at nanometer resolution. *Science* 313:1642–1645.
11. Rust MJ, Bates M, Zhuang X (2006) Sub-diffraction-limit imaging by stochastic optical reconstruction microscopy (STORM). *Nat Methods* 3:793–796.
12. Gustafsson MGL (2000) Surpassing the lateral resolution limit by a factor of two using structured illumination microscopy. *J Microsc* 198:82–87.
13. Agronskaia AV, et al. (2008) Integrated fluorescence and transmission electron microscopy. *J Struct Biol* 164:183–189.
14. Smith EA, et al. (2014) Quantitatively imaging chromosomes by correlated cryo-fluorescence and soft x-ray tomographies. *Biophys J* 107:1988–1996.
15. Chang YW, et al. (2014) Correlated cryogenic photoactivated localization microscopy and cryo-electron tomography. *Nat Methods* 11:737–739.
16. Liu B, et al. (2015) Three-dimensional super-resolution protein localization correlated with vitrified cellular context. *Sci Rep* 5:13017.

17. Sartori A, et al. (2007) Correlative microscopy: Bridging the gap between fluorescence light microscopy and cryo-electron tomography. *J Struct Biol* 160:135–145.
18. Arnold J, et al. (2016) Site-specific cryo-focused ion beam sample preparation guided by 3D correlative microscopy. *Biophys J* 110:860–869.
19. Schorb M, et al. (2017) New hardware and workflows for semi-automated correlative cryo-fluorescence and cryo-electron microscopy/tomography. *J Struct Biol* 197:83–93.
20. Le Gros M, McDermott G, Uchida M, Knoechel C, Larabell CA (2009) High-aperture cryogenic light microscopy. *J Microsc* 235:1–8.
21. Smith EA, et al. (2014) Correlative cryogenic tomography of cells using light and soft x-rays. *Ultramicroscopy* 143:33–40.
22. Le Gros M, Larabell CA (2006) Cryogenic immersion microscope. US Patent 7,852,554B2.
23. Nahmani M, Lanahan C, DeRosier D, Turrigiano GG (2017) High-numerical-aperture cryogenic light microscopy for increased precision of superresolution reconstructions. *Proc Natl Acad Sci USA* 114:3832–3836.
24. Edelstein AD, et al. (2014) Advanced methods of microscope control using μManager software. *J Biol Methods* 1:10.
25. Schindelin J, et al. (2012) Fiji: An open-source platform for biological-image analysis. *Nat Methods* 9:676–682.
26. Sage D, et al. (2017) DeconvolutionLab2: An open-source software for deconvolution microscopy. *Methods* 115:28–41.
27. Thevenaz P, Ruttimann U, Unser M (1998) A pyramid approach to sub-pixel registration based on intensity. *IEEE Trans Image Process* 7:27–41.